Restricted Nonlinear Scales of Turbulent Secondary Flows Over Spanwise Heterogeneous Roughness

Benjamin A. Minnick[a], Xiaowei Zhu[b], Dennice F. Gayme[a]

[a]*Department of Mechanical Engineering Johns Hopkins University, 3400 N. Charles St., Baltimore, MD, 21218, USA*
[b]*Atmospheric & Oceanography Science Princeton University, 300 Forrestal Rd., Princeton, NJ, 08540, USA*

Abstract

Recent studies, e.g., Wangsawijaya et al. (2020) have revealed the prevalence of streak meandering underlying turbulent flow over spanwise heterogeneous roughness. Here we exploit the scale decomposition inherent in the Restricted Nonlinear (RNL) modeling approach to further investigate this behavior. The RNL decomposition comprises a large-scale streamwise averaged mean with small-scale fluctuations about that mean defined through a dynamical restriction that leads to computational tractability. The simplified setting facilitates the study of secondary flow interacting with the large-scale streak via one-way coupling, thus enabling additional insight into relevant interaction mechanisms. In agreement with the experimental work, our results indicate that the energy of the large-scales is amplified over the low roughness region due to the secondary flow. The small-scales are shown to play a dominant role in the Reynolds stresses responsible for generation of the secondary flow. Conditional averaging of the RNL mean field reveals stronger momentum pathways and diminished energy over low roughness regions experiencing downwash in instances that differ from the time-averaged trends. Further analysis, via time-filtering, shows long time-scales pertinent to streak meandering are anti-correlated with instantaneous upwash/downwash motions that are the dominant contribution to the increased shear Reynolds stress observed over the low roughness strips.

Keywords: Turbulent Boundary Layers, Restricted Nonlinear, Secondary flows, Roughness

1. Introduction

The importance of coherent structures in the dynamics of turbulent boundary layers over smooth walls and homogeneous rough surfaces is well known. Early flow visualizations by Kline et al. (1967) revealed streamwise rolls and streaks near the wall. The dynamics of these structures and their interactions are responsible for the generation of skin-friction drag, see e.g. Raupach et al. (1991); Jiménez (2004). Near-wall streaks and rolls have also been shown to interact in a self-sustaining process (SSP) (Waleffe, 1997; Jeong et al., 1997), widely believed to be a dominant flow mechanism in wall-bounded turbulence.

Streamwise coherence also persists away from the wall, where early experiments identified turbulent bulges in the outer-layer (Fiedler and Head, 1966; Falco, 1977). Later works identified streamwise coherent large-scale or very-large-scale motions that lead to a secondary peak in the velocity spectra (Kim and Adrian, 1999; Marusic, 2001). These outer-layer structures interact with near-wall streaks by modulating their amplitude (Hutchins and Marusic, 2007; Mathis et al., 2011). Large scale streamwise vorticies and streaks have also been shown to interact in a SSP as part of the hierarchy of these cycles mirroring that of the near-wall steaks (Flores and Jiménez, 2010; Cossu and Hwang, 2016).

Similarities between flows over smooth walls and homogeneous rough surfaces readily permit methods to evaluate skin-friction drag for such surfaces by the Moody diagram or Hama roughness function (Nikuradse and Nikuradse, 1933; Moody, 1944; Hama et al., 1954). For example, streamwise coherent structures are spatially invariant over smooth walls and homogeneous roughness topography imposes similar stricture thereby permitting methods such as the Moody diagram or Hama roughness function to evaluate skin-friction drag independent of spatial orientation (Nikuradse and Nikuradse, 1933; Moody, 1944; Hama et al., 1954). Outer-layer similarity also enables estimates for turbulent statistics of flow over homogeneous rough walls (Townsend, 1980; Schultz and Flack, 2005; Flack et al., 2007). Unfortunately, when the roughness is not homogeneous, the mean velocity profiles and second-order statistics do not collapse at different spanwise locations (Medjnoun et al., 2018; Yang and Anderson, 2017; Chung et al., 2018).

The failure of Townsend's similarity hypothesis for such surfaces suggest that well established methods for characterization of flow over homogeneous roughness are not applicable to the wide range of heterogeneous surfaces

that are prevalent in nature and engineering applications. In fact, the full effects of such surfaces on the properties of turbulent flows over them has yet to be understood. Recent studies aimed at expanding the understanding of these flows have focused on how the topography affects their statistical features. In an early investigation along these lines, Barros and Christensen (2014) identify time-averaged alternating low- and high-momentum pathways (LMPs and HMPs respectively) flanked by streamwise vortices over a turbine blade eroded by foreign materials. This finding inspired others to study flow over more simplified spanwise heterogeneous topographies that have been shown to lead to the breakdown of self-similarity. Two classes of such surfaces are; ridge and strip roughness. Ridge roughness is characterized by alternating elevated and recessed regions of rough surfaces, i.e, the height of the surface varies in a regular pattern. Such surfaces have been constructed in experiments using alternating strips of Lego bricks with different heights (Vanderwel and Ganapathisubramani, 2015) as well as smooth surfaces of alternating heights (smooth ridges) (Medjnoun et al., 2018). Numerical studies typically implement this variation using immersed boundary methods (Hwang and Lee, 2018; Yang and Anderson, 2017; Awasthi and Anderson, 2018). In strip roughness, the height of the surface remains relatively constant and the heterogeneity arises from alternating strips of rough surfaces with different skin-friction. Experimental studies of turbulent boundary layers over strip roughness have been performed using densely packed gravel (Wang and Cheng, 2005) or sand paper (Bai et al., 2018; Wangsawijaya et al., 2020), while numerical studies have imposed spanwise variations in the wall-stress (Willingham et al., 2014; Chung et al., 2018).

There is a general consensus that the non-zero time-averaged streamwise vorticity that arises over spanwise heterogeneous rough surfaces is associated with the second kind of Prandtl's secondary flow (Prandtl, 1952); a notion that was investigated in detail in And (2015). This type of secondary flow is generated from spanwise variations in the Reynolds stresses that induce mixing in the cross-plane. This mixing generates spanwise varying regions comprised of high and low momentum pathways respectively forming between ridges or over ridges for ridge type roughness or over high and low roughness strips.

While much is known about the statistical features of secondary flow structures, their unsteady behavior was historically masked by the time-averaging employed in their analysis. Kevin et al. (2017) were the first to use correlations and conditional averaging to uncover meandering of sec-

ondary flow over herringbone riblets. The similarity of this behavior to that observed in smooth-walled turbulent boundary layers has led to a body of work exploring connections between these flows. For example, Kevin et al. (2019) attributed secondary flow meandering to an outer-layer streak-vortex instability mimicking one initially described near the wall (Jeong et al., 1997) and later at larger scales (Flores and Jiménez, 2010) of smooth wall turbulent flows. More specifically Kevin et al. (2019) argue that the streak-vortex instability model in Jeong et al. (1997) may provide structural model that could explain the meandering features in these flows. Zampiron et al. (2020) similarly found meandering of large-scale streaks (which they referred to as secondary current instability) over ridge roughness.

In strip type roughness Wangsawijaya et al. (2020) also found a secondary outer-layer in the streamwise energy spectra over the low roughness strip reminiscent of the outer-layer peak in the energy spectra found in experiment (Marusic, 2001) and simulation (Bernardini et al., 2014; Lee and Moser, 2015; Yamamoto and Tsuji, 2018) of smooth wall flows. The large-scale streaks found to modulate near-wall small-scales initially found in Hutchins and Marusic (2007) for a smooth wall flow, has also been found to occur in the LMPs over heterogeneous strip roughness (Awasthi and Anderson, 2018). Interestingly, these works have found the intensity of secondary flow meandering, energy amplification, and amplitude modulation to increase within the LMP. These studies certainly advance our understanding of coherent structures over heterogeneous strip roughness however questions remain, primarily, how do the secondary flow structures and large-scale streaks interact?

In this work we aim to further the understanding of these interactions using the restricted nonlinear (RNL) modeling framework, which provides a direct approach to isolate streak and vortex components and study their interactions. More specifically, the RNL representation decomposes the flow into a streamwise averaged mean component that is permitted to interact nonlinearly and perturbations whose nonlinear interactions are limited to those contributing to the mean. RNL turbulence is self-sustaining despite its reduced streamwise varying perturbation field (Thomas et al., 2014). The model also reproduces accurate turbulent statistics at moderate Reynolds numbers when the perturbation field is restricted to wavelengths that coincide with the outer-layer surrogate dissipation spectra (Minnick and Gayme, 2019). It has also been shown to be useful in the study of coherent structures, see e.g. Farrell et al. (2017); Gayme and Minnick (2019). The simplified setting of the RNL model provides a tractable simulation and analysis tool that

can be used to inform or analyse mechanistic models such as the streak-vortex instability (Jeong et al., 1997) based structural model that Kevin et al. (2019) postulated as a means to explain the meandering features in these flows.

We focus on turbulent flow over spanwise heterogeneous strip roughness and use RNL large eddy simulation (RNL-LES) model introduced in Bretheim et al. (2018) to study this flow at arbitrarily high Reynolds number. As in previous LES studies (Willingham et al., 2014) we impose the the strip roughness through the equilibrium wall-model boundary condition. First, we demonstrate that this reduced-order model predicts time-averaged secondary flow and momentum pathway trends consistent with observations in the literature. We then use the RNL decomposition to assess the contributions of the large-scale mean and small-scale perturbation field to the mixing and momentum transfer mechanisms. We examine the dynamics of the structures using a conditional averaging approach similar to that in Kevin et al. (2017). The results uncover similar meandering behavior, which suggests momentum mixing is primarily due to the secondary flow. Analysis by time-filtering the large-scale streamwise averaged mean component supports this conclusion and further shows streak motions and instantaneous upwash/downwash motions at long time-scales are highly anti-correlated contributing to increased outer-layer shear Reynolds stress.

2. The RNL-LES Model

We take (x, y, z) to denote the streamwise, wall-normal, and spanwise spatial coordinates with respective domain extents (L_x, L_y, L_z). t denotes the temporal coordinate. The total filtered velocity field, $\tilde{\mathbf{u}}_{\mathrm{T}}(x, y, z, t)$, is decomposed into a mean component, $\tilde{\mathbf{U}}(y, z, t) = \langle \tilde{\mathbf{u}}_T \rangle_x$, where the angle brackets with the subscript x indicate streamwise averaging, and a streamwise perturbation component, $\tilde{\mathbf{u}}(x, y, z, t)$. The governing equations consist of divergence free conditions, $\nabla \cdot \tilde{\mathbf{U}} = \nabla \cdot \tilde{\mathbf{u}} = 0$, and momentum equations,

$$\partial_t \tilde{\mathbf{U}} + \tilde{\mathbf{U}} \cdot \nabla \tilde{\mathbf{U}} + \nabla \tilde{P} + \nabla \cdot \langle \tau \rangle_x = -\langle \tilde{\mathbf{u}} \cdot \nabla \tilde{\mathbf{u}} \rangle_x,$$
$$\partial_t \tilde{\mathbf{u}} + \tilde{\mathbf{U}} \cdot \nabla \tilde{\mathbf{u}} + \nabla \tilde{p} + \nabla \cdot (\tau - \langle \tau \rangle_x) = -\tilde{\mathbf{u}} \cdot \nabla \tilde{\mathbf{U}},$$

which are derived from the filtered Navier-Stokes equations with nonlinear interactions between perturbations that do not result in a contribution to the mean omitted, i.e., $\langle \tilde{\mathbf{u}} \cdot \nabla \tilde{\mathbf{u}} \rangle_x - \tilde{\mathbf{u}} \cdot \nabla \tilde{\mathbf{u}} = 0$. This dynamical restriction leads to a simplified model in which structures with finite streamwise wavelengths

are isolated and only interact with the streamwise constant mean. Order reduction arises through the reduced streamwise wavenumber support of the perturbation dynamics, i.e. a small number of streamwise varying modes are simulated as described in (Bretheim et al., 2018).

In the context of flows over spanwise heterogeneous roughness, the advantage to expressing the filtered velocity field in this manner is the streak and vortex component are isolated, respectively expressed by the $\tilde{U}$ and $(\tilde{V}, \tilde{W})$ components. In the RNL decomposition, the streak component is independent of the x-position and is therefore only advected by the vortex component. Furthermore, the vortex component is only advected by itself. Both the streamwise averaged mean streak and vortex components are effectively forced by the streamwise perturbation field consistent with the SSP. No time-averaging operation is performed to derive the RNL equations and therefore the dynamics and the interactions between these components can be studied.

The sub-grid scale stress tensor is modelled using the standard Smagorinsky model (Smagorinsky, 1963) with an eddy viscosity formulation for the deviatoric component of this tensor

$$\boldsymbol{\tau} - \frac{1}{3}\mathrm{tr}(\boldsymbol{\tau})\boldsymbol{I} = -2\nu_e \tilde{\mathbf{S}}_{\mathrm{T}}.$$

Since the RNL methodology clearly defines streamwise scales in terms of large-scales represented by the streamwise averaged mean and small-scales as the streamwise varying perturbations, subgrid-scales in the cross-plane are modelled using the mean component. The eddy viscosity is therefore taken to be the product of the streamwise averaged filtered strain rate tensor,

$$\nu_e(y, z, t) = (C_s\Delta)^2 \sqrt{2\langle \tilde{\mathbf{S}}_{\mathrm{T}} \rangle_x : \langle \tilde{\mathbf{S}}_{\mathrm{T}} \rangle_x}.$$

Mason wall-damping is used for the Smagorinsky coefficient,

$$C_s\Delta = \Big[\Big(\frac{1}{C_0\Delta} \Big)^n + \Big(\frac{1}{\kappa(y + y_0(z))} \Big)^n \Big]^{-1/n},$$

with $n = 2$, von Kármán constant, $\kappa = 0.4$, and a spanwise varying roughness height y_0. The filter size is taken to be, $\Delta = (\Delta y \Delta z)^{1/2}$, instead of the traditional $\Delta = (\Delta x \Delta y \Delta z)^{1/3}$, and this requires that we use a slightly higher constant of $C_0 = 0.23$ rather than the common value of $C_0 = 0.16$ (Bretheim et al., 2018).

We impose the strip type spanwise heterogeneous roughness on the bottom boundary ($y = 0$) using the equilibrium wall-model with spanwise varying roughness heights $y_0(z)$, following previous LES studies of these flows (Willingham et al., 2014; And, 2015). The streamwise ($i = 1$) and spanwise ($i = 3$) components of the total wall-stress are prescribed as,

$$\tau_{i,2}^{(w)}(x, z, t) = -u_*^2 \frac{\tilde{u}_{T,i}(x, y_1, z)}{|\mathbf{U}|},$$

where y_1 is the first grid point from the wall,

$$u_*(z) = \frac{|\mathbf{U}|}{\log(y_1/y_0(z))}, \quad \text{and} \quad |\mathbf{U}|(z) = \sqrt{\tilde{U}_1^2(y_1, z) + \tilde{U}_3^2(y_1, z)}.$$

Note this equilibrium wall-model differs from the traditional wall-model used in LES in that the magnitude of the streamwise averaged mean component, $|\mathbf{U}|$ is used instead of the total velocity. The top boundary ($y = \delta$) is taken to be a stress-free, slip surface. Periodic boundary conditions are applied in the streamwise and spanwise directions.

3. Numerical Approach

Simulations are performed in a half channel configuration with domain extents $[L_x, L_y, L_z]/\delta = [2\pi, 1, 2\pi]$. The cross-plane grid resolution used for all simulations is $[N_y, N_z] = [144, 144]$. The non-zero streamwise wavenumber retained in the dynamics is $k_x\delta = 8$, and corresponds to a point in the outer-layer peak region of the vorticity spectra of an LES with equivalent grid resolution for a homogeneous rough wall configuration as detailed in Bretheim et al. (2018). Here the dimensional streamwise wavenumber is defined as $k_x = 2\pi n/L_x$ for some integer n.

The governing equations are solved in the pseudo-spectral code LESGO (https://lesgo.me.jhu.edu). Spectral derivatives are applied in the streamwise and spanwise directions, while second-order central finite differencing is used for wall-normal derivatives. The second-order explicit Adams-Bashforth method is used for time-marching. The 3/2-rule is used for dealiasing. The pressure Poisson equation is solved exactly by direct inversion in the streamwise and spanwise Fourier space, then discretizing the resulting ordinary differential equation using finite differencing in the wall-normal direction and applying the tri-diagonal matrix algorithm.

We take advantage of the reduced number of streamwise wavenumbers in the RNL-LES dynamics by solving the governing equations in (k_x, y, z, t) space. This involves computing the components of the nonlinear terms involving streamwise interactions as a convolution instead of as a product in physical space, which reduces the number of transforms required and saves computational time and resources, see Bretheim et al. (2018) for details or the implementation and computational savings.

We consider a topography of repeating units, each consisting of a high and low roughness strip with a total width of $S = (2\pi/3)\delta$. All simulations are three units wide. This topography is shown in the contour plot in Fig. 1, where black and white rectangles respectively indicate the high and low roughness regions. Within each unit the high roughness strip width is $\ell = 0.3125\ S$. This topography is imposed through the equilibrium wall-model described in equation 2 where $y_{0,h} = 0.001\delta$ for the high roughness and $y_{0,l} = 0.01 y_{0,h}$ for the low roughness. This particular topography was selected because secondary flows have been reported to be dominant for the spacing $S \sim \delta$ (Wangsawijaya et al., 2020) and the particular roughness heights, $y_{0,h}$ and $y_{0,l}$, are similar to those used in other LES studies, e.g. And (2015).

4. Results

The results section is outlined as follows. First the total RNL-LES velocity field, composed of the streamwise averaged mean and perturbation components, will be presented. The predicted time-averaged flow field will be compared to literature to confirm that this streamwise coherent structure based reduced-order model is capable of predicting HMP/LMP and secondary flow trends in a time-averaged sense. Second, the RNL-LES model components will be decomposed and investigated to isolate the contributions from the large-scale streamwise averaged mean and small-scale streamwise perturbations. The remainder of the results section focuses on large-scale streak meandering. For this part of the paper, we first perform a conditional averaging analysis to assess the RNL-LES model's ability to predict meandering behavior. We then investigate interactions between the secondary flow and the meandering of streaks using time-filtering of the streamwise averaged mean component of the RNL-LES field.

4.1. The Total RNL-LES Velocity Field

Fig. 1a compares time-averaged streamwise velocity profiles obtained from RNL-LES of homogeneous roughness at the low and high roughness levels ($y_{0,l}$ and $y_{0,h}$) to those obtained over the low and high roughness strips for the spanwise heterogeneous surface. These profiles show similar behavior to experimental and numerical studies, see e.g., And (2015). Near the wall the low and high roughness strips show similar velocity predictions to their corresponding homogeneous roughness counterparts, a consequence of the boundary condition imposed. Further from the wall these profiles mix in the cross (y, z)-plane such that the velocity profile over the high roughness strip increases and attains a higher velocity compared to the homogeneous case. Similarly for the profile over the low roughness strip which attains a lower velocity than compared to the homogeneous case far from the wall.

The contour plot in Fig. 1b provides a cross-stream view of the time-averaged flow with arrows indicating vectors of spanwise/wall-normal flow directions (secondary flow). Here the full spanwise variation of the streamwise velocity profiles are visualized, where it is clear that HMPs and LMPs are observed over the high and low roughness regions respectively. The arrows show that the formation of these pathways is highly dependent on the secondary flow. A pair of time-averaged streamwise rolls with alternating directions is observed for each high/low roughness region, centered at $y \approx \delta/2$. The location and orientation of this secondary flow is comparable to results reported in And (2015), as is the intensity, visualized using the swirl strength in Fig. 1c. The ability of the RNL-LES model to accurately predict the time-averaged secondary flow and corresponding momentum pathways is a result of the streamwise constant nonlinearity retained in the model dynamics.

Fig. 2 shows a three dimensional perspective of an instantaneous snapshot of the streamwise velocity field at the mid-plane of the half-channel. Here the boundaries of the high roughness regions are indicated by solid black lines. At $y \approx \delta/2$ where the secondary flow is dominant, high and low speed streaks are shown to align with high and low roughness regions respectively. Although these high and low speed large-scale structures are organized preferentially over the respective roughness regions, they meander instantaneously - a phenomenon first demonstrated by in Kevin et al. (2017). Among these large-scale streaks, a single small-scale streamwise wavelength, represented by the perturbation component, is shown to be prevalent. This perturbation component, which is loosely coupled to the mean, is thought

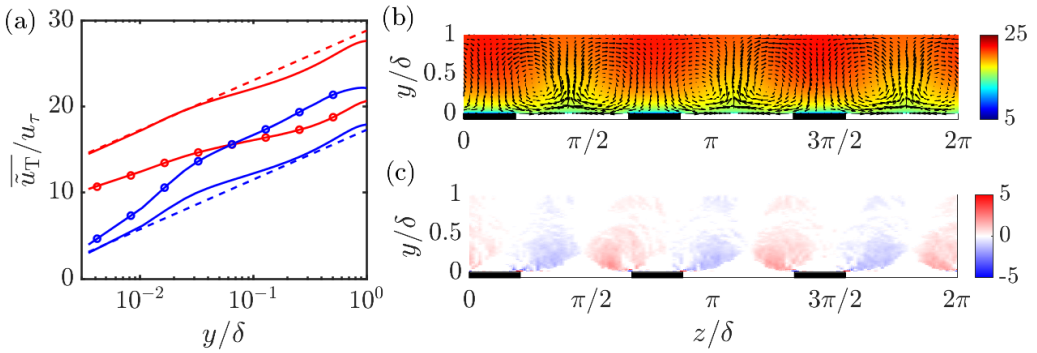

Figure 1: Time-averaged velocity field predictions from the RNL-LES model. (a) Solid lines are homogeneous roughness predictions at $y_0/\delta = 10^{-5}$ (red) and $y_0/\delta = 10^{-3}$ (blue) with corresponding dashed lines: $(1/0.4)\log(y/y_0)$. Solid lines with markers are heterogeneous roughness predictions taken at spanwise locations centered over low (red) and high (blue) roughness strips. (b) Contours of the time averaged streamwise velocity field with arrows indicating cross-stream velocity field (v, w components) superimposed. (c) Swirl strength contour. Markers in (a) and arrows in (b) do not represent grid resolution.

to re-energize the large-scale streaks. In the cross-plane, the sum of these components is shown to produce multi-scale behavior.

The time-averaged and instantaneous characteristics of the RNL-LES total velocity field discussed above indicated that this reduced-order model is capable of predicting salient features of turbulent boundary layers over spanwise heterogeneous roughness. The turbulence is self-sustaining, despite the limited number of streamwise Fourier modes simulated, suggesting spanwise heterogeneous roughness does not significantly alter the RNL SSP, as anticipated. Furthermore the level of agreement of the time-averaged statistics with And (2015) indicates the selected perturbation modes suitable for homogeneous roughness in the RNL-LES model is also suitable for spanwise heterogeneous roughness. This indicates outer-layer similarity can potentially be applied to small dissipative streamwise scales even if it cannot be applied to turbulent statistics, although further analysis is required to fully explore this notion and rigorously prove this conjecture.

The interactions retained in the streamwise averaged mean equation of the RNL-LES model are analogous to those considered in the inviscid two-dimensional three-velocity component model of Jeong et al. (1997), which is the basis of a structural model proposed by Kevin et al. (2017). The streamwise averaged mean streak, U, is only advected by the streamwise averaged

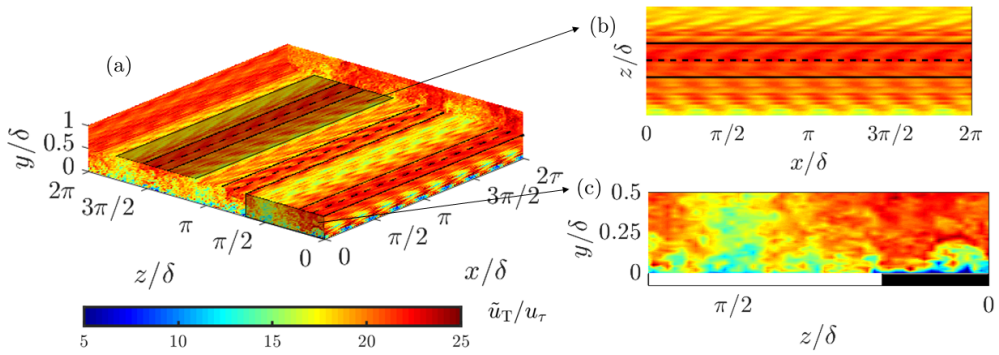

Figure 2: Instantaneous snapshot of the streamwise velocity field at the mid-plane ($y/\delta = 0.5$) of the half-channel. Thick black lines in panel (a) show the borders of the high roughness regions centered at the black dashed lines. Shaded regions in panel (a) are shown up close in panels (b) and (c). The xz-plane in (b) is taken at height $y = \delta/2$.

mean vortex, consisting of cross-plane components V, W, and forms momentum pathways. The vortex component is not advected by U and generates the secondary flow. Meandering characteristics of this streak-vortex interaction will be discussed in later sections. The next section will continue to investigate interactions between the streamwise averaged mean and perturbation components of the RNL-LES model.

4.2. Decomposition of the RNL-LES Field

Fig. 3 shows an instantaneous cross-stream snapshot of the RNL-LES streamwise velocity field alongside the contributions from its mean and perturbation components. The cross-plane snapshots in the top row of the figure indicate that, as expected, the streamwise averaged (RNL) mean velocity acts as a large-scale in that it filters small scale activity. Although the perturbation field is supported by a single streamwise wavenumber, full scale variation is observed in the cross-plane. The intensity of the perturbation component is particularly high in the region over the high roughness strip. The RNL mean component is further decomposed into a time-average, $\overline{\widetilde{U}}$, and fluctuation, $\tilde{U}'$, components in the bottom row of Fig. 3. Note that since time-averaged quantities are independent of streamwise location, $\overline{\widetilde{u}_T} = \overline{\widetilde{U}}$ and $\overline{\widetilde{u}} = 0$. This decomposition reveals that while the time-fluctuating component of the streamwise average mean contributes to the total fluctuations, it still comprises larger cross-plane scales than the perturbation component.

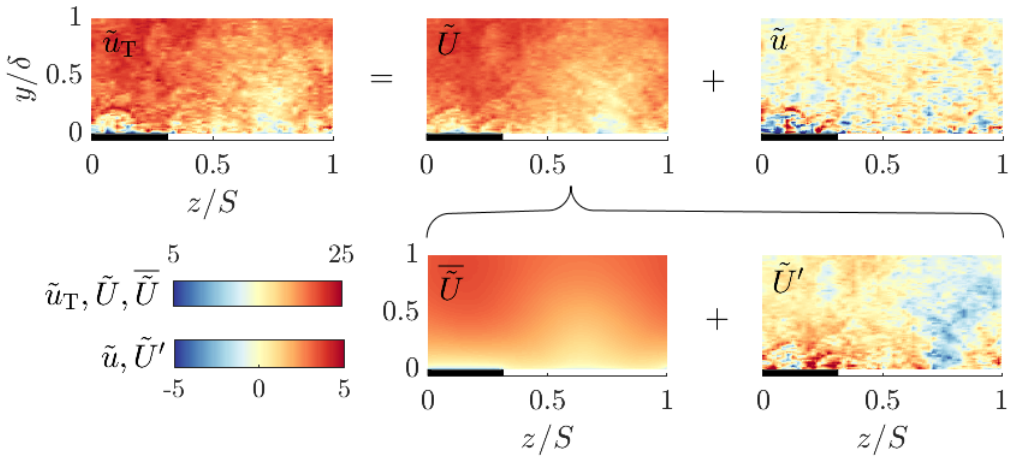

Figure 3: Instantaneous streamwise velocity field, $\tilde{u}_\mathrm{T}$ decomposed into the streamwise averaged mean, $\tilde{U}$, and streamwise varying perturbation, $\tilde{u}$, components. The mean component is further decomposed into a time-average, $\overline{\tilde{U}}$, and fluctuation, $\tilde{U}'$, component. All quantities are non-dimensionalized by u_τ.

This supports the characterization that the RNL mean component represents the large scales.

We now further explore the contributions of the mean and perturbation components to the flow statistics. Fig. 4 shows the normal and uv Reynolds stresses alongside their relative contributions from the mean and perturbation components. For comparison, Reynolds stress predictions over homogeneous high roughness are included to the left of each panel and for homogeneous low roughness to the right. Fig. 5 provides the Reynolds stresses generated by the spanwise heterogeneity that are otherwise negligible in flows over homogeneous roughness.

Since both the mean and perturbation components of the RNL model are time-fluctuating, they both contribute to the total Reynolds stress which is found to show reasonable agreement with And (2015). Furthermore with only two streamwise wavenumbers, $k_x\delta = 0, 8$, simulated in the RNL-LES model these results are equivalent to modelled one-dimensional spectra varying in the spanwise and wall-normal directions. Therefore Reynolds stresses involving the streamwise averaged mean effectively represent spectra from cumulative large-scales, while Reynolds stresses involving streamwise perturbations represent spectra from small-scales.

The large-scale component of the streamwise Reynolds stress, $\overline{\tilde{U}'\tilde{U}'}$, in

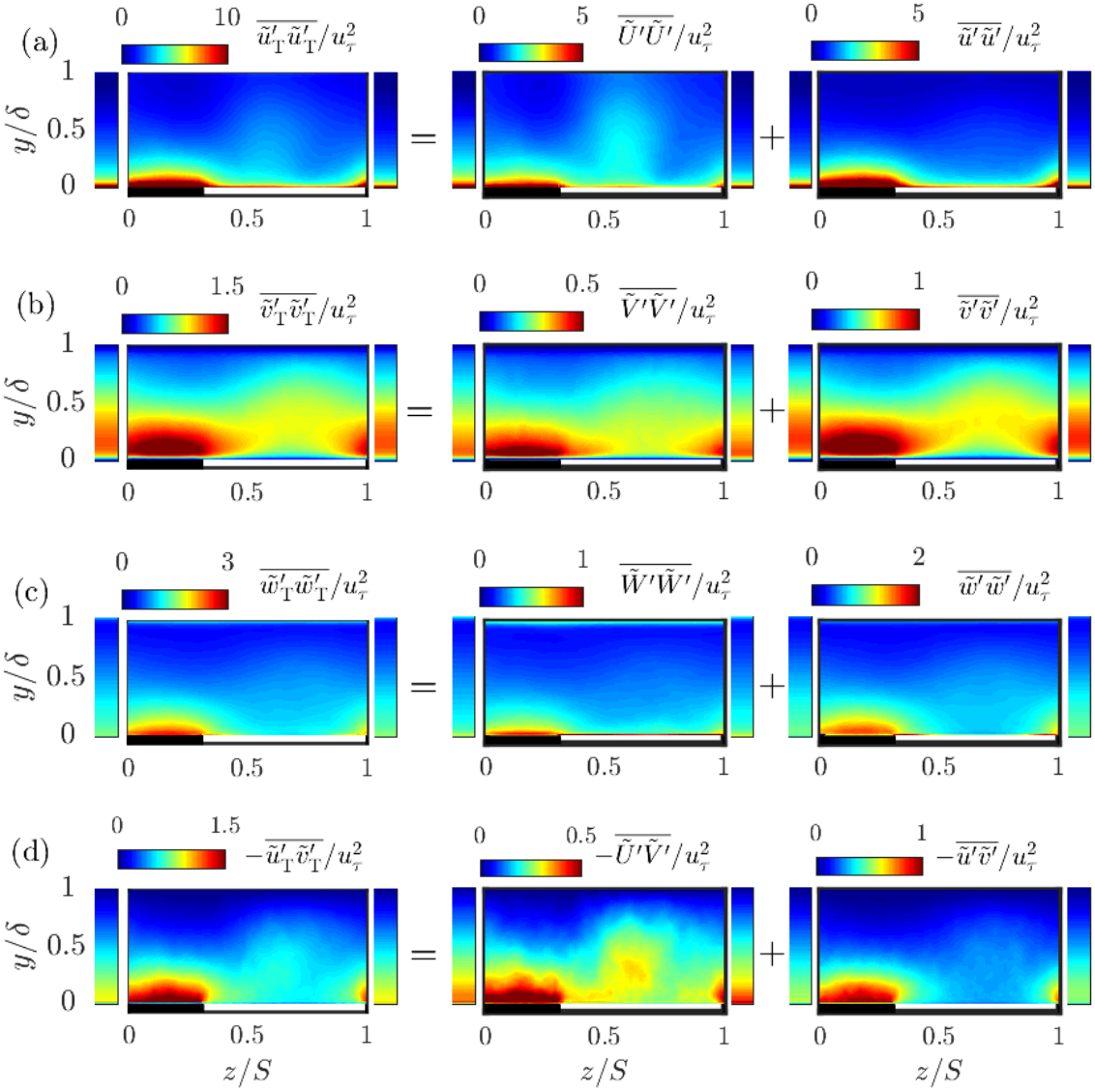

Figure 4: Total Reynolds stress decomposed into RNL-LES streamwise averaged mean (large-scale) and streamwise varying perturbation (small-scale) components. Reynolds stresses shown are also relevant in homogeneous cases. To the left of all heterogeneous roughness contours is the corresponding high roughness homogeneous prediction, similarly to the right is the low roughness homogeneous prediction. Results are shown for one of the repeating roughness units. Note the color maps for each plot are given and vary to highlight the gradation in intensity for each case.

Fig. 4a shows higher energy in the outer-layer over the low roughness region near the center of the time-averaged secondary flow. This is particularly evident if one examines the trend in the homogeneous cases, which shows a more rapid decrease in energy with distance from the wall. This finding is consistent with observations in the experimental work of Wangsawijaya et al. (2020), which suggests the secondary flow supplies additional energy to the very large-scale motions. The small-scale component, $\overline{\tilde{u}'\tilde{u}'}$, contributes little to this outer-layer energy. The small-scales instead show higher magnitude near the wall and peak over the high roughness region.

A similar trend is observed for the dominant Reynolds stress that acts in the streamwise momentum equation, $\overline{\tilde{u}'_{\mathrm{T}}\tilde{v}'_{\mathrm{T}}}$, shown in panel (d). This panel shows that, as expected, the small-scale perturbations have a greater exchange of momentum in the near wall region and the large-scale mean exchanges momentum further from the wall. Similar to the streamwise Reynolds stress, a larger exchange of momentum is observed further from the wall over the low roughness strip, particularly in the mean component, indicating the large-scale secondary motions enhance mixing in this region. Comparing this behavior to the analogous Reynolds stress predictions from the homogeneous roughness cases indicates that the mixing induced by the spanwise heterogeneity increases the cross-Reynolds stress directly over the high roughness strip, near the wall, but lowers the cross-Reynolds stress over the low roughness strip near the wall. This trend holds regardless of streamwise scale.

The small-scale perturbation component of the normal Reynolds stresses involving cross-plane velocity components in panels (b) and (c) of Fig. 4 are shown to have higher contributions to the overall stress than the large-scale mean component, which is also observed for the homogeneous roughness cases. Unlike the $\overline{\tilde{U}'\tilde{U}'}$ and $\overline{\tilde{U}'\tilde{V}'}$ stresses, there is no discernible outer-layer peak that is only identified in the large-scale mean component. Similar to the cross-Reynolds stress, the mixing induced by the spanwise heterogeneity increases these normal Reynolds stresses over the high roughness strip and decreases it over the low roughness strip near the wall. The stress then increases over the low roughness strip far from the wall.

Fig. 5 shows that the $\overline{\tilde{v}'_{\mathrm{T}}\tilde{w}'_{\mathrm{T}}}$ Reynolds stress is of significance as its gradients are responsible for the production of the secondary flow; a conclusion consistent with that of And (2015). The RNL decomposition of this Reynolds stress reveals the small-scale component, $\overline{\tilde{v}'\tilde{w}'}$, is dominant, particularly near

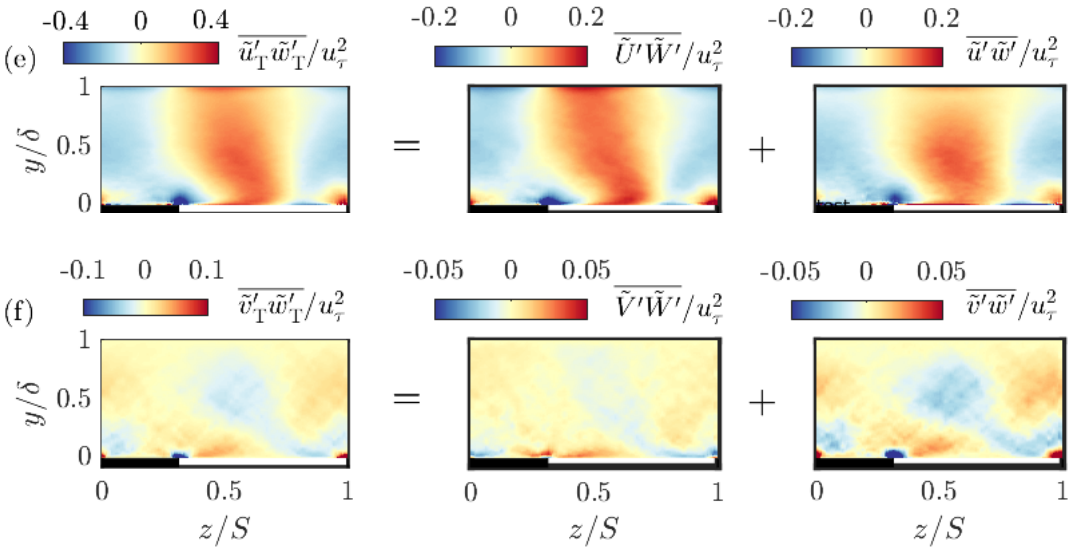

Figure 5: Total Reynolds stress decomposed into RNL-LES streamwise averaged mean (large-scale) and streamwise varying perturbation (small-scale) components. Reynolds stresses shown are negligible in homogeneous cases. Results shown over one repeating roughness unit. Note the color maps for each plot are given and vary to highlight the gradation in intensity for each case.

the wall at the roughness transition. The sharp sign change in this Reynolds stress at the roughness transition is not observed in the large-scale component, $\overline{\tilde{V}'\tilde{W}'}$, suggesting only small-scales play a role in the generation of secondary flow. Both large-scale streamwise averaged mean and small-scale streamwise perturbation components contribute to the $\overline{\tilde{u}'_{\mathrm{T}}\tilde{w}'_{\mathrm{T}}}$ Reynolds stress and show a similar trend.

The findings in Figs. 4 and 5 support conclusions made in numerical and experimental studies of the statistical behavior of turbulent flow over spanwise heterogeneous roughness. The decomposition of the RNL model is shown to be particularly appealing in assessing large and small scale contributions to outer-layer turbulent energy and secondary flow generation.

We now turn our attention to the time-varying aspects of the flow and relate meandering features of the large-scale streamwise averaged mean flow field to recent studies of turbulent flows over spanwise heterogeneous roughness Kevin et al. (2017); Zampiron et al. (2020).

4.3. Conditional Averaging

The previous section demonstrated that the streamwise average mean of the RNL decomposition enables structural features of the large-scale momentum pathways and secondary flow to be interrogated directly. We next exploit this feature by performing a conditional averaging analysis to illustrate streak meandering and other features masked by time-averaging. Following the procedure introduced in Kevin et al. (2017), we sort instantaneous flow samples according to the direction of the locally averaged wall-normal velocity of the large-scale streamwise averaged mean centered over a high roughness region and the two neighboring low roughness regions. The spanwise boundaries of the areas over which these local averages are performed, are indicated by solid black lines in Fig. 6. The center location of the region is indicated by the dashed black line. The local averages are performed over the entirety of the corresponding roughness region and the wall-normal extent. It should be noted that this analysis can be sensitive to the chosen width of the local averages, and the one chosen here is larger than the one used in Kevin et al. (2017). However the overall trends illustrating the secondary flow direction and streak meandering are reasonably insensitive to this choice and therefore will remain relatively unaffected.

Fig. 6 shows the results from this conditional averaging across a total of 70,000 samples organized into four bins respectively shown in panels (a)–(d): bin 1 (+,-,+), bin 2 (-,-,+), bin 3 (+,-,-), and bin 4, which includes the other five combinations. Here the +/- sign is used to denote the upward/downward direction of the locally averaged wall-normal velocity of the RNL mean component in each region. The order of the combination denotes the location of each local average, from left to right: over the low roughness strip, the high roughness strip, and then the other low roughness strip. Included in this figure is the percentage of samples used to develop each conditional average, this percentage indicates the frequency of occurrence for each case. Additionally, we denote the spanwise position in these figures as z_c, taking $z_c = 0$ to denote the center of the high roughness region and $z_c = \pm 0.5S$ to indicate the center of the neighboring low roughness regions.

The case (+,-,+) which is most comparable to the time-average velocity field is shown to be predominant, more-so than the case considered in Kevin et al. (2017), this is likely due to the choice of conditional averaging width. Regardless, it is clear that a flow behavior different than the time-averaged sense occurs relatively often. Similar to the results in Kevin et al. (2017), cases where downwash exists simultaneously over the high roughness region

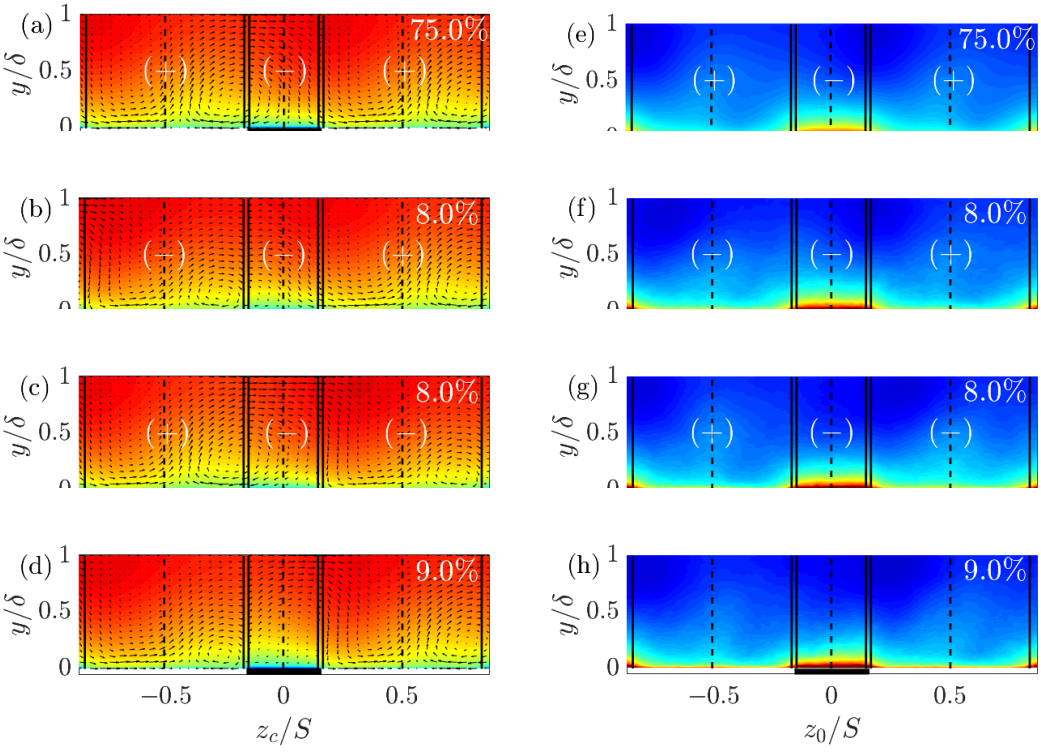

Figure 6: Conditionally averaged (a-d) velocity field and (e-h) $\overline{\tilde{U}'\tilde{U}'}/u_\tau^2$ based on direction of locally averaged wall-normal velocity performed over the entire high roughness region (indicated by black rectangle) and low roughness regions (centered by solid black line and bounded by dotted lines). Direction of flow in these regions indicated by +/- respectively denoting upwash/downwash. All five other possible combinations [(+,+,+),(+,+,-),(-,+,+),(-,+,-),(-,-,-)] not shown in panels (a-c,e-g) are included in (d,h). Color bar for streamwise velocity contour same as Fig. 2 and for $\overline{\tilde{U}'\tilde{U}'}/u_\tau^2$ as in Fig. 4.

and a neighboring low roughness region, i.e., those denoted (-,-,+) and (+,-,-), occur often.

The downwash region of the (-,-,+) and (+,-,-) cases continue to show a time-averaged vortex, however it is reduced in size and magnitude. Interestingly, the streamwise momentum in this region is notably higher than the overall time-average field indicating a conditionally averaged HMP between the high and low roughness region coinciding with the conditionally averaged downwash.

Included in Fig. 6 is the streamwise Reynolds stress of the large-scale RNL mean component. Panels (e)–(h) are binned following the same convention as panels (a)–(d). The (-,-,+) and (+,-,-) cases show an asymmetry in the $\overline{\tilde{U}'\tilde{U}'}$ profiles over the neighboring low roughness strips which is not seen in the other cases in panels (e) and (h). A higher streamwise Reynolds stress far from the wall is predicted over the low roughness strip with corresponding upwash or conditionally averaged LMP. This behavior suggests that the outer-layer peak is intensified within an instantaneous upwash region and diminished in an instantaneous downwash region as the secondary flow meanders. A similar trend is observed in conditionally averaged $\overline{\tilde{U}'\tilde{U}'}$ statistics (not shown here).

The meandering of the secondary flow in the RNL framework is a result of the streamwise component of the mean equation, U responding to the secondary flow, (V, W), acting as a passive scalar only subject to small-scale forcing. In other words, streak meandering and secondary flow have a one-way coupling where the secondary flow drives streak meandering. This coupling is imposed in the RNL mean, but given the similarity in behavior observed in experiments this type of coupling may persist in the full system, evaluating this idea is a topic of ongoing work. In the next section we further investigate the interaction between the meandering secondary flow that drives the streak by reviewing a time history of the streamwise averaged mean component far from the wall, where the secondary flow is dominant.

4.4. Large-Scale Meandering

Results in the previous section have highlighted time-varying features resolved by the RNL-LES model that are similar to those observed in the experiments of Kevin et al. (2017). In this section, we expand our study to investigate connections between meandering in the momentum pathways and these time-varying motions of the secondary flow. Consistent with our analysis in section 4.3, we consider only the streamwise averaged mean component

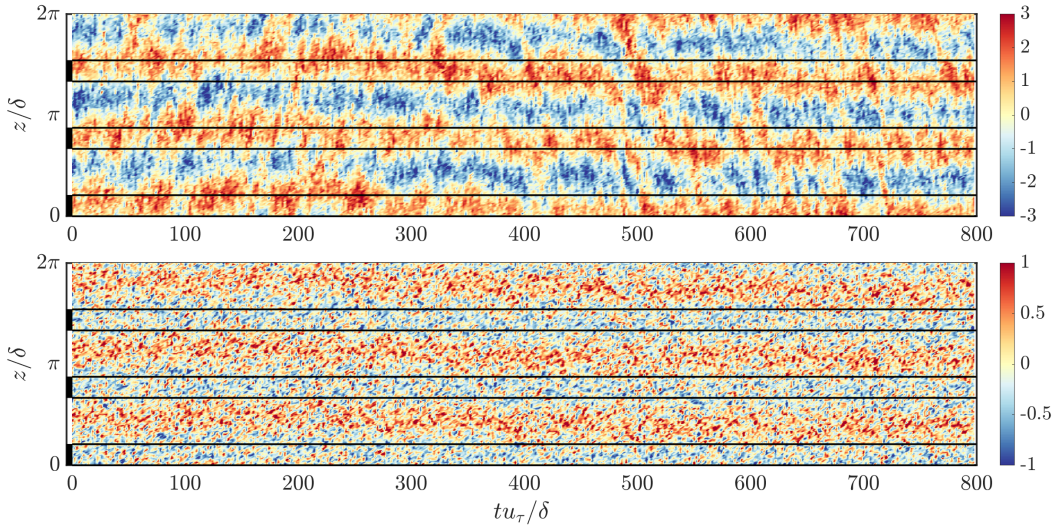

Figure 7: Time and spanwise variations of the streamwise averaged mean velocity field at $y = \delta/2$: (a) streamwise component, $(\tilde{U} - \langle\overline{\tilde{U}}\rangle_z)/u_\tau$, and (b) wall-normal component, $(\tilde{W} - \langle\overline{\tilde{W}}\rangle_z)/u_\tau$ EDIT SUBMITTED VERSION – THIS SHOULD BE V NOT W. The spanwise average component is removed to show streak meandering near the roughness strips.

of the RNL-LES model, as it allows us to isolate the large-scale streamwise elongated structures believed to meander (Kevin et al., 2019; Wangsawijaya et al., 2020).

Fig. 7, shows the time evolution of fluctuations of the RNL mean minus the spanwise average $(\tilde{U} - \langle\overline{\tilde{U}}\rangle_z)$ at the channel center $\delta/2$. Here the high roughness strip locations are outlined by the black lines. This figure clearly shows the large scale meandering of the streamwise (panel (a)) and wall-normal (panel (b)) velocity components over the roughness strips. Consistent with the spanwise-varying time-averaged field, $\overline{\tilde{U}}$, shown in Fig. 3, higher streamwise velocity fluctuations primarily occur over the high roughness strips. This high momentum streak however is shown to meander over the neighboring low roughness region at various points in time. Time fluctuations in the upwash and downwash regions over the respective low and high roughness strips are noted in the wall-normal component of this velocity field. Both the streamwise and wall-normal velocity components show small time-scale fluctuations. However, a large time-scale fluctuation is evident in the streamwise velocity component. These larger time-scales, on the order

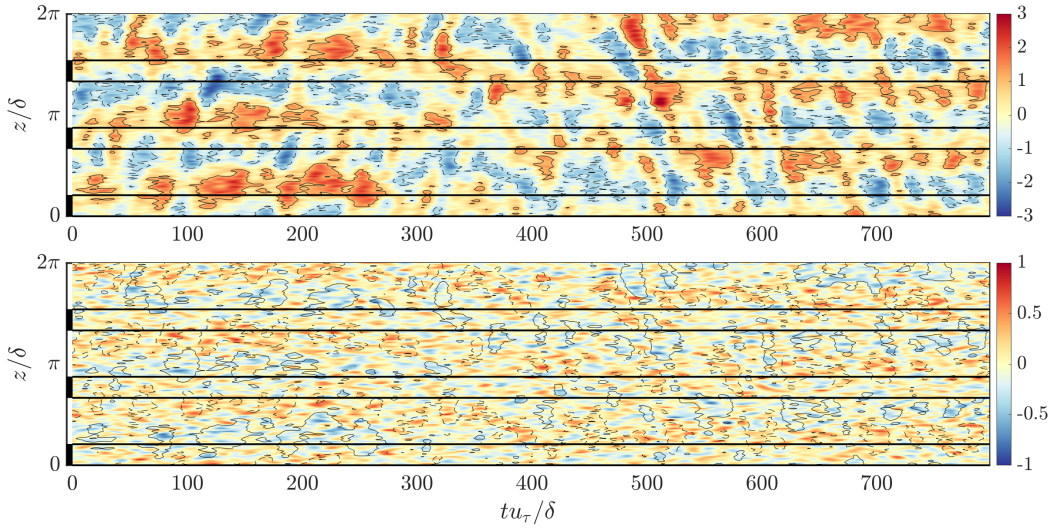

Figure 8: Filtered time fluctuations of the streamwise averaged mean velocity at $y = \delta/2$: (a) streamwise component and (b) wall-normal component. Time-scales smaller than $\delta/\langle\overline{U}\rangle_z(y = \delta/2) = 0.05$ are filtered out to isolate large-scale streak meandering. Black solid line contours indicate streamwise velocity fluctuations that are $1u_\tau$ greater than the average and black dotted line contours indicate streamwise fluctuations that are $1u_\tau$ less than average.

of $\sim 10\delta/u_\tau$ and greater, are of interest here because meandering is expected to occur over large time-scales.

In order to further investigate the evolution of the large scales we time-filter the data such that only time-scales above $\delta/\langle\overline{\tilde{U}}\rangle_z(y = \delta/2) = 0.05$ (corresponding to $\langle\overline{\tilde{U}}\rangle_z = 20\ u_\tau$) are retained. Fig. 8 plots the filtered streamwise and wall-normal components of the streamwise averaged (RNL) mean velocity field over the same time window shown in Fig. 7. Here, it is clear that the time-filtering process effectively smooths the velocity fields and filters out small time scale turbulent fluctuations. However, we do not remove the spanwise average, so the meandering in the momentum pathways that was prominent in Fig. 7 is less evident. The contours shown indicate fluctuations that are faster (positive) and slower (negative) than the average flow (corresponding to zero fluctuations). We highlight fluctuations with magnitudes u_τ above the average value using a black contour line, and those one u_τ below the average using a dotted black contour. The figure shows that there are several events where downward ($\tilde{V}' < 0$) fluctuations occur

during fast streamwise fluctuations ($\tilde{U}' > 0$). Similarly, upward motions occur during slow streamwise fluctuations. These events occur more frequently and with higher intensities over the LMPs, which is a trend consistent with the $\overline{\tilde{U}'\tilde{V}'}$ spectra in Fig. 4. This anti-correlation between streamwise and wall-normal velocity fluctuations is persistent at the long time-scales, only for the streamwise averaged mean component of the RNL-LES model and provides additional evidence for the secondary peak in the co-spectra over low roughness strips.

Referring to the time-averaged flow, where upwash occurs on average over the low roughness strips, Fig. 8 suggests fast streamwise velocity fluctuations often occur when the instantaneous secondary flow opposes the time-averaged secondary flow and slow streamwise velocity fluctuations occur when the instantaneous secondary flow intensifies. It is interesting to note that this phenomena, resolved by the RNL-LES model, occurs via one-way coupling where the large-scale streamwise velocity component does not interact with the large-scale wall-normal component. This suggests secondary flow meandering induces streak meandering and their coupled effect increases the turbulent Reynolds stress $\overline{u'_{\mathrm{T}}v'_{\mathrm{T}}}$ within the LMP.

5. Conclusion

An RNL-LES model is shown to reproduce the momentum pathways formed from secondary flow induced by spanwise heterogeneous strip roughness. The natural scale decomposition of this framework is then exploited to isolate the role of large and small streamwise scales in these secondary motions. An analysis of scale dependent streamwise Reynolds stress indicates that large-scale low speed streaks over the low roughness accumulate energy from the secondary flow. The small-scale component of the $\overline{\tilde{v}'_{\mathrm{T}}\tilde{w}'_{\mathrm{T}}}$ Reynolds stress is observed to be dominant near the wall at the roughness transition, suggesting small-scales are primarily responsible for the generation of the secondary flow.

Conditional averaging based on the direction of the wall-normal velocity of the RNL mean component over the low and high roughness regions is performed to quantify streak meandering. Upwash over low roughness regions and downwash over the high roughness region, as observed in the time-averaged flow field, is predominant however not the only instance observed. The other cases, that occur approximately a quarter of the time,

show less intense secondary flow coinciding with an intensified streamwise momentum streak.

The conditional averaging predictions from the RNL-LES model inspired an analysis of the time history of the streamwise and wall-normal velocity components of the streamwise averaged (RNL) mean field. Further filtering of motions with respect to time revealed streak meandering is closely related to the instantaneous secondary flow. High speed motions were shown to occur when the secondary flow was moving downward, and similarly secondary flow was directed upward during low speed motions. This trend occurs often over long time-scales and is a dominant contribution to increased outer-layer $\overline{\tilde{U}'\tilde{V}'}$ Reynolds stress. Furthermore, this observation occurs with higher intensity over the low roughness strips where meandering is found to be dominant.

The RNL dynamics appears to provide a minimal representation of the streak-vortex instability model described in Jeong et al. (1997) and reasoned to be the mechanism for outer-layer streak meandering in spanwise heterogeneous roughness (Kevin et al., 2019). The construction of the RNL model and its ability to reproduce this meandering suggests a one-way coupling wherein secondary flow leads to meandering. Further analysis of this interaction is a direction of ongoing work.

Further investigation of the role of small-scales and their response to streak meandering using the RNL perturbation component is another potential direction for future study. In particular, for the cases of varying high roughness width to low roughness width ratio to discussed inWangsawijaya et al. (2020), where the spanwise wavelength of the roughness was varied.

6. Acknowledgements

We gratefully acknowledge support from the National Science Foundation (CBET 1652244) and the Office of Naval Research (N00014-20-1-2535). This work was carried out at the Advanced Research Computing at Hopkins (ARCH) core facility (rockfish.jhu.edu), which is supported by the National Science Foundation (NSF) grant number OAC 1920103.

References

, 2015. Numerical and experimental study of mechanisms responsible for turbulent secondary flows in boundary layer flows over spanwise heterogeneous roughness. J. Fluid Mech. 768, 316–347.

Awasthi, A., Anderson, W., 2018. Numerical study of turbulent channel flow perturbed by spanwise topographic heterogeneity: Amplitude and frequency modulation within low- and high-momentum pathways. Phys. Rev. Fluids 3, 044602.

Bai, H., Kévin, Hutchins, N., Monty, J.P., 2018. Turbulence modifications in a turbulent boundary layer over a rough wall with spanwise-alternating roughness strips. Phys. Fluids 30, 055105.

Barros, J.M., Christensen, K.T., 2014. Observations of turbulent secondary flows in a rough-wall boundary layer. J. Fluid Mech. 748, R1.

Bernardini, M., Pirozzoli, S., Orlandi, P., 2014. Velocity statistics in turbulent channel flow up to $Re_\tau = 4000$. J. Fluid Mech. 742.

Bretheim, J.U., Meneveau, C., Gayme, D.F., 2018. A restricted nonlinear large eddy simulation model for high Reynolds number flows. Journal of Turbulence 19, 141–166.

Chung, D., Monty, J.P., Hutchins, N., 2018. Similarity and structure of wall turbulence with lateral wall shear stress variations. J. Fluid Mech. 847, 591–613.

Cossu, C., Hwang, Y., 2016. Self-sustaining processes at all scales in wall-bounded turbulent shear flows. Phil. Trans. R. Soc. A 375, 20160088.

Falco, R.E., 1977. Coherent motions in the outer region of turbulent boundary layers. Physics of Fluids 20, 124–132.

Farrell, B.F., Gayme, D.F., Ioannou, P.J., 2017. A statistical state dynamics approach to wall turbulence. Phil. Trans. R. Soc. A 375, 20160081.

Fiedler, H., Head, M.R., 1966. Intermittency measurements in the turbulent boundary layer. J. Fluid Mech. 25, 719–735.

Flack, K.A., Schultz, M.P., Connelly, J.S., 2007. Examination of a critical roughness height for outer layer similarity. Phys. Fluids 19, 095104.

Flores, O., Jiménez, J., 2010. Hierarchy of minimal flow units in the logarithmic layer. Phys. Fluids 22, 071704.

Gayme, D.F., Minnick, B.A., 2019. Coherent structure-based approach to modeling wall turbulence. Phys. Rev. Fluids 4, 110505.

Hama, F., of Naval Architects, S., Engineers, M., 1954. Boundary-layer Characteristics for Smooth and Rough Surfaces, by Francis R. Hama.

Hutchins, N., Marusic, I., 2007. Evidence of very long meandering features in the logarithmic region of turbulent boundary layers. J. Fluid Mech. 579, 1–28.

Hwang, H.G., Lee, J.H., 2018. Secondary flows in turbulent boundary layers over longitudinal surface roughness. Phys. Rev. Fluids 3, 014608.

Jeong, J., Hussain, F., Schoppa , W., Kim, J., 1997. Coherent structure near the wall in a turbulent channel flow. Journal of Fluid Mechanics 332, 185 – 214.

Jiménez, J., 2004. Turbulent flows over rough walls. Annu. Rev. Fluid Mech. 36, 173–196.

Kevin, K., Monty, J., Hutchins, N., 2019. Turbulent structures in a statistically three-dimensional boundary layer. J. Fluid Mech. 859, 543–565.

Kevin, K., Monty, J.P., Bai, H.L., Pathikonda, G., Nugroho, B., Barros, J.M., Christensen, K.T., Hutchins, N., 2017. Cross-stream stereoscopic particle image velocimetry of a modified turbulent boundary layer over directional surface pattern. J. Fluid Mech. 813, 412–435.

Kim, K.J., Adrian, R.J., 1999. Very large scale motion in the outer layer. Phys. Fluids 11, 417–422.

Kline, S.J., Reynolds, W.C., Schraub, F.A., Runstadler, P.W., 1967. The structure of turbulent boundary layers. J. Fluid Mech. 30, 741–773.

Lee, M., Moser, R.D., 2015. Direct numerical simulation of turbulent channel flow up to $Re_\tau = 5200$. J. Fluid Mech. 774, 395–415.

Marusic, I., 2001. On the role of large-scale structures in wall-turbulence. Phys. Fluids 13. doi:10.1063/1.1343480.

Mathis, R., Hutchins, N., Marusic, I., 2011. A predictive inner-outer model for streamwise turbulence statistics in wall-bounded flows. J. Fluid Mech. 681, 537–566.

Medjnoun, T., Vanderwel, C., Ganapathisubramani, B., 2018. Characteristics of turbulent boundary layers over smooth surfaces with spanwise heterogeneities. Journal of Fluid Mechanics 838, 516–543.

Minnick, B.A., Gayme, D.F., 2019. Characterizing energy transfer in restricted nonlinear wall-bounded turbulence, in: International Symposium on Turbulence and Shear Flow Phenomena (TSFP-11).

Moody, L., 1944. Friction factors for pipe flow. Trans. ASME 66, 671–677.

Nikuradse, J., Nikuradse, J., 1933. Laws of flow in rough pipes. VDI Forschungsheft , 361.

Prandtl, L., 1952. Essentials of Fluid Dynamics. Hafner Publishing Company.

Raupach, M.R., Antonia, R.A., Rajagopalan, S., 1991. Rough-Wall Turbulent Boundary Layers. Appl. Mech. Rev. 44, 1–25.

Schultz, M.P., Flack, K.A., 2005. Outer layer similarity in fully rough turbulent boundary layers. Exp. Fluids 38, 328–340.

Smagorinsky, J., 1963. General circulation experiments with the primitive equations: I. the basic experiment. Monthly Weather Review 91, 99 – 164.

Thomas, V.L., Lieu, B.K., Jovanović, M.R., Farrell, B.F., Ioannou, P.J., Gayme, D.F., 2014. Self-sustaining turbulence in a restricted nonlinear model of plane couette flow. Phys. Fluids 26, 105112.

Townsend, A.A.R., 1980. The structure of turbulent shear flow. Cambridge university press.

Vanderwel, C., Ganapathisubramani, B., 2015. Effects of spanwise spacing on large-scale secondary flows in rough-wall turbulent boundary layers. J. Fluid Mech. 774, R2.

Waleffe, F., 1997. On a self-sustaining process in shear flows. Phys. Fluids 9, 883–900.

Wang, Z.Q., Cheng, N.S., 2005. Secondary flows over artificial bed strips. Advances in Water Resources 28, 441–450.

Wangsawijaya, D.D., Baidya, R., Chung, D., Marusic, I., Hutchins, N., 2020. The effect of spanwise wavelength of surface heterogeneity on turbulent secondary flows. J. Fluid Mech. 894, A7.

Willingham, D., Anderson, W., Christensen, K.T., Barros, J.M., 2014. Turbulent boundary layer flow over transverse aerodynamic roughness transitions: induced mixing and flow characterization. Phys. Fluids 26, 025111.

Yamamoto, Y., Tsuji, Y., 2018. Numerical evidence of logarithmic regions in channel flow at $\mathrm{Re}_\tau = 8000$. Phys. Rev. Fluids 3, 012602.

Yang, J., Anderson, W., 2017. Numerical study of turbulent channel flow over surfaces with variable spanwise heterogeneities: Topographically-driven secondary flows affect outer-layer similarity of turbulent length scales. Flow, Turbulence and Combustion 100, 1–17.

Zampiron, A., Cameron, S., Nikora, V., 2020. Secondary currents and very-large-scale motions in open-channel flow over streamwise ridges. Journal of Fluid Mechanics 887, A17.